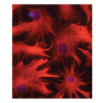

Massive CO_2 Ice Deposits Sequestered in the South Polar Layered Deposits of Mars

Roger J. Phillips *et al.*

Science **332**, 838 (2011);
DOI: 10.1126/science.1203091

25. J. Urbano *et al.*, *Organometallics* **24**, 1528 (2005).
26. E. Despagnet-Ayoub *et al.*, *Organometallics* **27**, 4779 (2008).
27. J. Urbano *et al.*, *Organometallics* **28**, 5968 (2009).
28. J. M. DeSimone, E. Tumas, Eds., *Green Chemistry Using Liquid and Supercritical Carbon Dioxide* (Oxford Univ. Press, Oxford, 2003).
29. Materials and methods are available as supporting material on *Science* Online.
30. M. P. Doyle, M. A. McKervey, T. Ye, *Modern Catalytic Methods for Organic Synthesis with Diazo Compounds* (Wiley, New York, 1998).
31. A. Caballero, A. Prieto, M. M. Diaz-Requejo, P. J. Pérez, *Eur. J. Inorg. Chem.* **2009**, 1137 (2009).
32. S. J. Blanksby, G. B. Ellison, *Acc. Chem. Res.* **36**, 255 (2003).
33. E. Nakamura, N. Yoshikai, M. Yamanaka, *J. Am. Chem. Soc.* **124**, 7181 (2002).
34. A. A. C. Braga *et al.*, *Organometallics* **25**, 5292 (2006).
35. A reviewer mentioned the possibility of the involvement of radical species. Extensive previous work favors the metallocarbene route [see (*19*) and references therein]. Moreover, these experiments were carried out in a vessel that was neither purged nor vented; therefore, 100 mL of air was present in the reaction mixture. The oxygen contained in that volume would preclude the conversion of any radical into the desired product. See (*36*).
36. G. Asensio, R. Mello, M. E. González-Núñez, C. Boix, J. Royo, *Tetrahedron Lett.* **38**, 2373 (1997).

Acknowledgments: We dedicate this work to Professor Ernesto Carmona. Support for this work was provided by the Ministerio de Ciencia e Innovación (grants CTQ2008-00042-BQU, CTQ2007-65251-BQU, and CTQ2007-30762-E), the European Research Area Chemistry Programme (2nd call "Chemical activation of carbon dioxide and methane" contract no. 1736154), the Consolider Ingenio 2010 (grants CSD2006-003 and CSD2007-00006), the Institut de Chimie of the CNRS, the Junta de Andalucía (P07-FQM-2870), and the Generalitat Velenciana (ACOMP/2010/155). We thank the Servicio Central de Soporte a la Investigación Experimental (Universidad de Valencia) for access to the instrumental facilities and J. de la Rosa and A. Sánchez de la Campa (Universidad de Huelva) for ICP-MS analyses.

Supporting Online Material
www.sciencemag.org/cgi/content/full/332/6031/835/DC1
Materials and Methods
SOM Text
Figs. S1 to S7
Tables S1 and S2
References *25*, *26*, and *37*

10 February 2011; accepted 19 March 2011
10.1126/science.1204131

Massive CO_2 Ice Deposits Sequestered in the South Polar Layered Deposits of Mars

Roger J. Phillips,[1]* Brian J. Davis,[2]† Kenneth L. Tanaka,[3] Shane Byrne,[4] Michael T. Mellon,[5] Nathaniel E. Putzig,[2] Robert M. Haberle,[6] Melinda A. Kahre,[7] Bruce A. Campbell,[8] Lynn M. Carter,[9] Isaac B. Smith,[10] John W. Holt,[10] Suzanne E. Smrekar,[11] Daniel C. Nunes,[11] Jeffrey J. Plaut,[11] Anthony F. Egan,[12] Timothy N. Titus,[3] Roberto Seu[13]

Shallow Radar soundings from the Mars Reconnaissance Orbiter reveal a buried deposit of carbon dioxide (CO_2) ice within the south polar layered deposits of Mars with a volume of 9500 to 12,500 cubic kilometers, about 30 times that previously estimated for the south pole residual cap. The deposit occurs within a stratigraphic unit that is uniquely marked by collapse features and other evidence of interior CO_2 volatile release. If released into the atmosphere at times of high obliquity, the CO_2 reservoir would increase the atmospheric mass by up to 80%, leading to more frequent and intense dust storms and to more regions where liquid water could persist without boiling.

The martian atmosphere is dominated by CO_2 with an annual mean pressure currently about 6 mbar (6 hPa) (*1*), although early in the planet's history CO_2 likely existed at the ~1 bar level. Some of this ancient atmospheric CO_2 may be stored in the polar layered deposits (PLD) (*2*), although, it is now thought, only in modest quantities. The water-ice–dominated southern PLD (SPLD) presently host a small [<5-m thick, ~90,000 km^2 (*3*)] perennial CO_2-ice deposit (*4*) overlying a thin water-ice layer (*5*), which together compose the south pole residual cap (SPRC). If the SPRC CO_2 material were to be released completely into the atmosphere, the increase in pressure would be only a few tenths of a mbar and insufficient to buffer the atmospheric CO_2 during changing climatic conditions (*5*). Here, we use radar-sounder data to show that the volume of sequestered CO_2 in the SPLD is substantially larger than previously believed, competing in magnitude with the present atmospheric abundance.

SHARAD (Shallow Radar) is a sounding radar on the Mars Reconnaissance Orbiter (MRO) mission (*6*), and its results are displayed in radargrams with axes of time delay and orbital position (Fig. 1). Previous mapping of subsurface reflectors by SHARAD in the north PLD (NPLD) revealed a crisp radar stratigraphy to the base of the deposits (*7*, *8*). For the SPLD, the radar signal does not penetrate the deposits as deeply as in the NPLD, and in only a limited number of places is there a well-defined stratigraphy (*9*). There are some regions with nearly reflection-

[1]Planetary Science Directorate, Southwest Research Institute, Boulder, CO 80302, USA and Department of Earth and Planetary Sciences, Washington University, St. Louis, MO 63130, USA. [2]Department of Space Studies, Southwest Research Institute, Boulder, CO 80302, USA. [3]Astrogeology Science Center, U.S. Geological Survey, Flagstaff, AZ 86001, USA. [4]Lunar and Planetary Laboratory, University of Arizona, Tucson, AZ 85721, USA. [5]Laboratory for Atmospheric and Space Physics, University of Colorado, Boulder, CO 80303, USA. [6]Space Science and Astrobiology Division, National Aeronautics and Space Administration (NASA) Ames Research Center, Moffett Field, CA 94035, USA. [7]Bay Area Environmental Research Institute/NASA Ames Research Center, Moffett Field, CA 94035, USA. [8]Center for Earth and Planetary Studies, Smithsonian Institution, Washington, DC 20013, USA. [9]Science and Exploration Directorate, NASA Goddard Space Flight Center, Greenbelt, MD 20771, USA. [10]Institute for Geophysics, Jackson School of Geosciences, University of Texas, Austin, TX 78758, USA. [11]Jet Propulsion Laboratory, California Institute of Technology, Pasadena, CA 91109, USA. [12]Department of Space Operations, Southwest Research Institute, Boulder, CO 80302, USA. [13]Department of Information Engineering, Electronics and Telecommunications, Sapienza University of Rome, 18-00184 Rome, Italy.

*To whom correspondence should be addressed. E-mail: roger@boulder.swri.edu
†Present address: Department of Geophysics, Colorado School of Mines, Golden, CO 80401, USA.

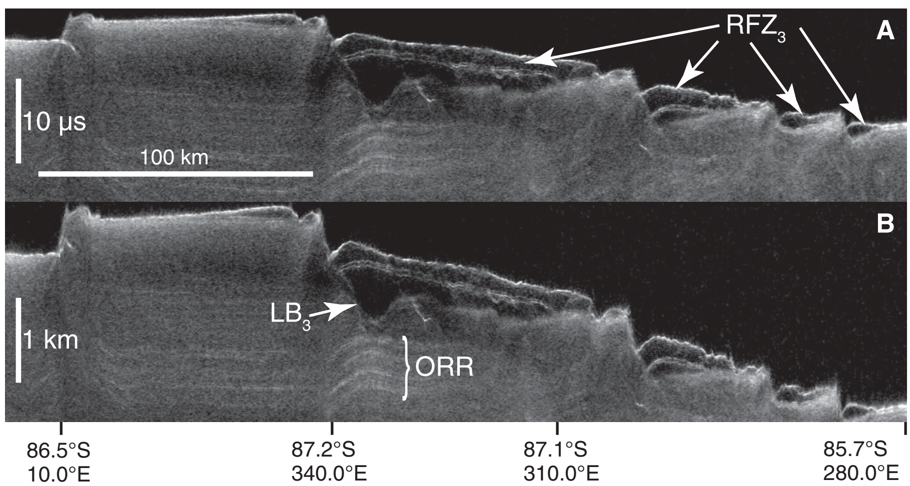

Fig. 1. SHARAD radargram 5968-01 traversing RFZ_3 terrain shown in original time-delay format (**A**) and converted to depth (**B**) by using the permittivity of water ice. Ground track location is shown in Fig. 3. ORR and LB_3 are indicated.

free subsurface zones (RFZ) extending downward from near the surface to depths approaching 1 km (fig. S1). The RFZs can be subdivided into four distinct types and locations (table S1) on the basis of their radar characteristics; here, we focus on RFZ_3, which is spatially coincident with the SPRC. Except for a commonly occurring thin layer that bisects the unit (Fig. 1), RFZ_3 is the most reflection-free volume that we have seen on Mars with SHARAD data: the signal level within approaches the background noise. Deeper reflectors passing beneath RFZ_3 brighten slightly more than expected on the basis of the change in thickness of typical SPLD material, implying that RFZ_3 deposits attenuate a radar signal less severely than these typical regions. Importantly, the low-power RFZ_3 radar return is thus not caused by strong scattering or absorption losses within the deposit.

To determine the real permittivity (ε') of RFZ_3, we mapped key SHARAD reflectors for 79 MRO orbits (fig. S2). The lower boundary of RFZ_3, LB_3, is a highly irregular buried erosional surface that truncates subhorizontal reflectors. Extending several hundred meters beneath RFZ_3 is a zone of unorganized, weak radar reflectors that in turn is underlain by a coherent sequence of organized (layered) radar reflectors (ORR). By using the a priori assumption of a bulk water-ice composition ($\varepsilon' = 3.15$) for the SPLD, we converted the vertical axis of radargrams from time delay to depth. The converted ORR sequence beneath LB_3 is typically offset from surrounding regions and exhibits significant topographic variations (Fig. 1B) that are strongly anticorrelated with LB_3 (Fig. 2A). This anticorrelation is unexpected because there is very likely no geological link between the earlier deposition of the ORR and the later erosion of the material above it that was subsequently filled with RFZ_3 material [see (*10*) for details]. On the basis of the argument that the anticorrelations are the fortuitous result of an incorrect choice of ε' for RFZ_3, we found for each radargram the ε' value that gave zero correlation between LB_3 and a test reflector (TR) in the ORR sequence (Fig. 2, B and C) (*10*). A second method (*10*) sought to minimize topographic perturbations and offsets on the TR by finding the ε' value that obtained the smallest residuals to a linear regression on this interface (Fig. 2, D and E). Both methods tended to produce a relatively smooth and subhorizontal disposition to the TR, similar in nature to the likely extension of ORR observed by SHARAD in the Promethei Lingula region (*9*). Forty-one of the 79 radargrams were suitable for quantitative analyses using these procedures, and by using different strategies we found mean values for ε' of the RFZ_3 volume in the range of 2.0 to 2.2, with standard deviations of 0.1 to 0.2 (*10*).

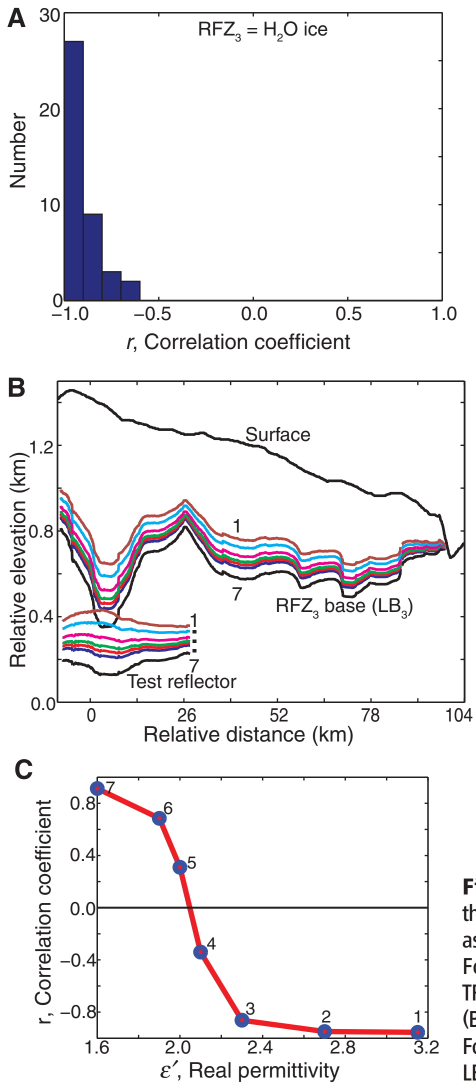

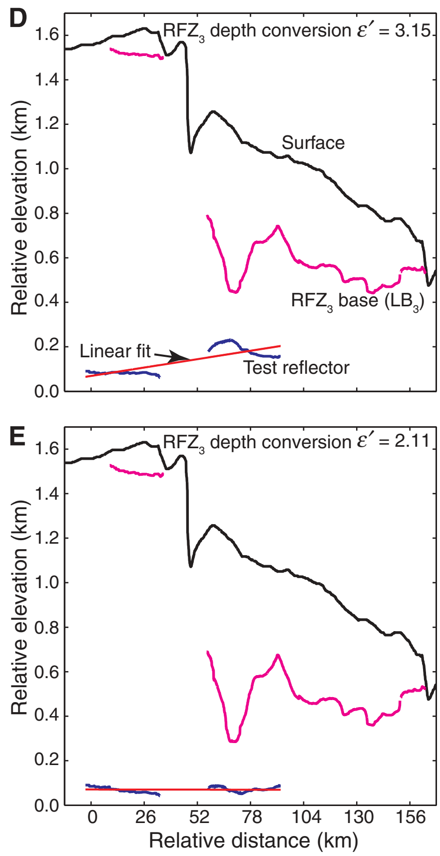

Fig. 2. (**A**) Distribution for 41 orbital observations of the correlation coefficients between LB_3 and the TR assuming RFZ_3 ε' equals that of water ice, 3.15. (**B**) For observation 8104-01, the positions of LB_3 and TR as a function of RFZ_3 ε'. (**C**) The ε' values used in (B) and the corresponding correlation coefficients. (**D**) For observation 8104-01, the positions of the surface, LB_3, and TR for RFZ_3 $\varepsilon' = 3.15$. (**E**) Same as (D) except RFZ_3 $\varepsilon' = 2.11$, which gives the best-fitting linear regression on TR.

These permittivity estimates for RFZ_3 are unexpectedly close to a laboratory-measured value of low-porosity CO_2 ice of 2.12 ± 0.04 (*11*), similar to the well-known frequency-independent value of about 2.2 for bulk dry ice (*12*). The SHARAD-derived permittivity values are substantially lower than those of water ice (3.15) and CO_2 clathrate-hydrate ice (~2.85) (*13*), strongly supporting the hypothesis that RFZ_3 is a solid CO_2 deposit. An alternative view that RFZ_3 is porous water ice can be rejected on the basis of permittivity-thickness relationships (*10*).

With the permittivities estimated, we converted the time delays through RFZ_3 (using $\varepsilon' = 2.1$) to thicknesses over each of the 79 radar traverses (fig. S3) and by interpolation constructed a continuous thickness distribution. Figure 3 shows this result placed over a geological map showing stratigraphic units in a portion of the SPLD (*14*, *15*). Of interest here are the largely overlapping horizontal extents of the $A{\small A}_3$ unit and the successively overlying water-ice ($A{\small A}_{4a}$) and CO_2-ice ($A{\small A}_{4b}$) units making up the SPRC. Also shown are the contacts (dashed) for unit $A{\small A}_3$, with the locations constrained well by exposures in troughs and by partial exposures beneath the SPRC. Where SHARAD data are available, there is a remarkable spatial correlation of RFZ_3 to the $A{\small A}_3$ unit except for the extremes of northward-extending lobes of the unit (*16*). Thus, we propose that the $A{\small A}_3$ unit is in fact RFZ_3, and its composition is dominated by CO_2 ice.

The $A{\small A}_3$ unit contains a system of large troughs, up to several km wide and typically <100 m deep, that do not cut older units (Fig. 3). In turn, smaller parallel aligned ridges, troughs, and elongate depressions mark some of these large troughs, and in places the depressions appear as coalescing or elongated pits (Fig. 4). Additionally, the westernmost outcrops of unit $A{\small A}_3$ (north of 87°S and near 240° to 270°E) include about 20 rimless circular pits (~300- to ~4000-m diameter), which do not occur in layers underlying unit $A{\small A}_3$ and do not display any rims or ejecta. All of these smaller troughs, depressions, and pits appear to result from erosion and removal of unit $A{\small A}_3$, with a strong component of sublimation and collapse. These features are not found elsewhere in the SPLD, and the CO_2-ice layer ($A{\small A}_{4b}$) of the SPRC is the only other perennial

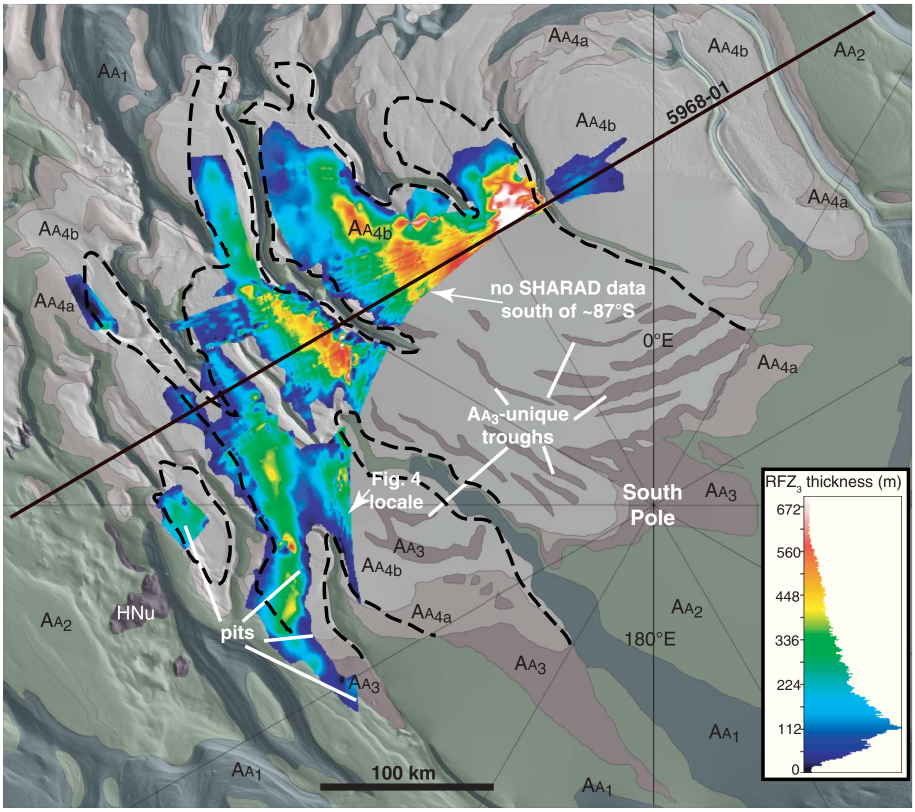

Fig. 3. Polar stereographic map of a portion of the SPLD, showing RFZ_3 thickness variations interpolated to a continuous volume for the 79 SHARAD ground tracks where RFZ_3 deposits were observed. Bright colors indicate deposit thicknesses calculated by using $\varepsilon' = 2.1$, and the histogram (**inset**) provides their relative occurrences. Base map (subdued colors) shows SPLD stratigraphy (*14*, *15*) with geologic units from oldest to youngest: HNu (substrate underlying SPLD); AA_1 (evenly bedded layers, up to 3.5 km thick); AA_2 (evenly bedded layers, <300 m thick); AA_3 (~300 m thick); and AA_{4a} and AA_{4b} (water-ice and CO_2-ice members, respectively, of the SPRC). The units are separated by unconformities, indicating episodes of erosion between them that resulted in retreat of the original lateral extents of the units and in development of local troughs and depressions. Dashed lines indicate boundaries of unit AA_3 where partially buried. Mars Orbiter Laser Altimeter (MOLA) shaded relief base at 115 m per pixel; because of spacecraft orbital inclinations, no SHARAD or MOLA data are available poleward of ~87°S. Ground track of observation 5968-01 (Fig. 1) is shown.

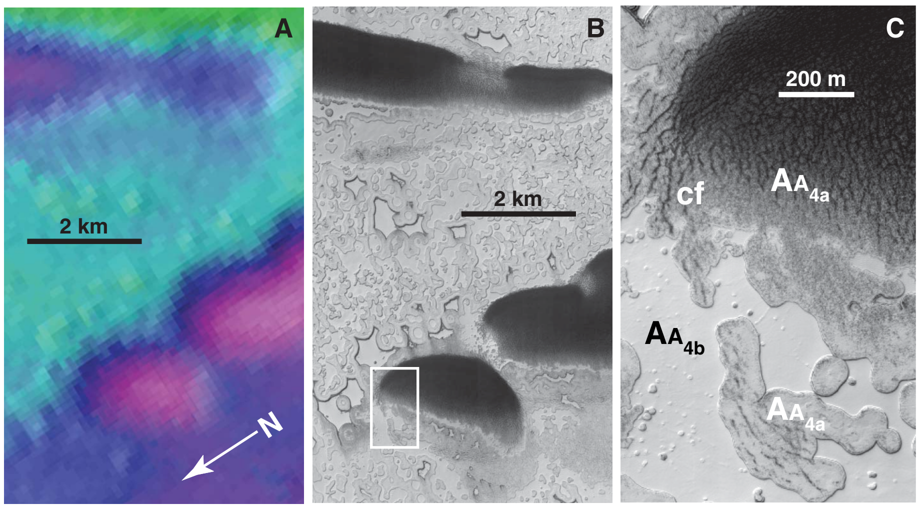

Fig. 4. MOLA topographic image (**A**) in the vicinity of 87°S, 268°E, showing linear depressions or troughs in the AA_3 unit. The total elevation range of the image is ~75 m from the lowest (pink) to the highest (green) surface. The troughs are associated with circular pits [(**B**), part of MRO HiRISE (High Resolution Imaging Science Experiment) image ESP_014342_0930] and are thinly buried by the SPRC (**C**), with unit AA_{4b} (CO_2 ice) displaying sublimation windows into a fractured water-ice unit AA_{4a} beneath (northwestern corner of a pit). The water-ice layer is completely exposed in the northeastern portion of this pit, where intense polygonal fracturing gives way to concentric fracturing on the pit rim (cf).

unit in the SPLD that exhibits clear (although different) morphological indicators of sublimation (*5*). The lack of sublimation features in exposures of the older units AA_1 and AA_2 indicate that CO_2, and not H_2O, is the sublimating material in the AA_3 unit, as might be expected given their relative volatilities. The AA_3 unit within pits distributed along the linear depressions is covered by a heavily fractured SPRC water-ice layer (AA_{4a}) that is overlain in places by the sublimating SPRC CO_2 layer (AA_{4b}) that formed after the fracturing (Fig. 4). The fracturing, not found in other SPLD units, may be a response to continuing unit AA_3 sublimation after the pits had first formed. The other three RFZs lack surface expressions of sublimation, but nondetection of sufficiently rugged lower boundaries precluded permittivity estimates.

Because we equate RFZ_3 to unit AA_3, we used the areal distribution of the geological unit to extrapolate the RFZ_3 volume poleward of ~87°S, achieving a total volume range (*17*) of ~9500 to 12,500 km^3 (*10*). In contrast, the volume of the CO_2-dominated SPRC is less than 380 km^3 (*3*), about 30 times less. The RFZ_3 thickness-independent permittivity values (*10*) imply a density close to that of bulk dry ice, 1500 to 1600 kg m^{-3} (*18*), which converts volume to an equivalent atmospheric pressure of 4 to 5 mbar, up to ~80% of the equivalent mass in the current atmosphere. The collapse features in the AA_3 unit suggest that the RFZ_3 mass has been waning, and an isolated patch of RFZ_3 (at ~345°E in Figs. 1 and 3) appears to be an erosional remnant. This suggests that the atmosphere has contained less than the present ~6 mbar of CO_2, hinting at past atmospheric collapse.

The lack of reflections in RFZ_3 apart from the bisecting layer can be interpreted as a lack of dust (*7*). Global climate models (GCMs) suggest (*19*) that, when the obliquity of Mars drops below a critical value, the atmosphere collapses onto the polar caps. At low obliquities, the ability of the atmosphere to lift dust is greatly diminished (*20*), possibly providing an explanation for the radar observations. Obviously, the CO_2 now buried in RFZ_3 was in the atmosphere at some time in the past. A plausible assumption is that the RFZ_3 mass was largely in the atmosphere when the insolation at the south pole at summer solstice was at a maximum, which for the past one million years occurred about 600,000 years ago [obliquity = 34.76°, eccentricity = 0.085, longitude of perihelion = 259.4° (*21*)].

To assess the impact on some first-order climate parameters, we ran a fast version of the NASA/Ames Mars GCM (version 1.7.3) for these orbital conditions with a total exchangeable CO_2 inventory (atmosphere plus caps) equal to the present inventory (7.1 mbar) plus 5 mbar. We found that most of the additional 5 mbar of CO_2 ended up in the atmosphere. Surface pressures rose uniformly around the planet, with global-mean annually averaged pressures equaling 10.5 mbar. Annual mean cap masses increased by about 0.8 mbar, not accounting for the lost RFZ_3 mass. Surface temperatures, however, decreased slightly (~0.7 K) because the CO_2 ice was on the ground for a longer period, and this compensated the modest greenhouse effect.

There are two implications of these changes in the climate system. First, the increased CO_2 pressure expands the geographic locations where these pressures exceed the triple-point pressure of water, thereby permitting liquid water to persist without boiling (although it may still evaporate, as on Earth) (*22*). Second, higher surface pressures will lead to higher surface wind stresses, which will loft more dust in the atmosphere, leading to an increase in dust storm frequency and intensity. Given the complex interplay between the dust, water, and CO_2 cycles, additional changes in the climate system are very likely.

References and Notes

1. B. M. Jakosky, R. J. Phillips, *Nature* **412**, 237 (2001).
2. R. B. Leighton, B. C. Murray, *Science* **153**, 136 (1966).
3. P. C. Thomas, P. B. James, W. M. Calvin, R. Haberle, M. C. Malin, *Icarus* **203**, 352 (2009).
4. H. Kieffer, *J. Geophys. Res.* **84**, 8263 (1979).
5. S. Byrne, A. P. Ingersoll, *Science* **299**, 1051 (2003).
6. R. Seu *et al.*, *J. Geophys. Res.* **112**, E05S05 (2007).
7. R. J. Phillips *et al.*, *Science* **320**, 1182 (2008); 10.1126/science.1157546.
8. N. E. Putzig *et al.*, *Icarus* **204**, 443 (2009).
9. R. Seu *et al.*, *Science* **317**, 1715 (2007).
10. Materials and methods are available as supporting material on *Science* Online.
11. E. Pettinelli *et al.*, *J. Geophys. Res.* **108**, 8029 (2003).
12. R. Simpson, B. Fair, H. Howard, *J. Geophys. Res.* **85**, 5481 (1980).
13. D. C. Nunes, R. J. Phillips, *J. Geophys. Res.* **111**, E06S21 (2006).
14. E. J. Kolb *et al.*, "The residual ice cap of Planum Australe, Mars: New insights from the HRSC experiment." Paper presented at the 37th Lunar and Planetary Science Conference, League City, TX, 13 to 17 March 2006; www.lpi.usra.edu/meetings/lpsc2006/pdf/2408.pdf.
15. K. L. Tanaka, E. Kolb, C. Fortezzo, "Recent advances in the stratigraphy of the polar regions of Mars." Paper presented at the Seventh International Conference on Mars, Pasadena, CA, 9 to 13 July 2007; www.lpi.usra.edu/meetings/7thmars2007/pdf/3276.pdf.
16. RFZ_3 is seen discontinuously in radargrams here, but key reflectors could not be mapped with high confidence likely because of surface scattering interference, resolution limitations, and lack of coverage.
17. A lower value of ~4000 to 4500 km^3 is obtained with the unlikely assumption that RFZ_3 does not extend beyond SHARAD's data gathering locales, which are limited by MRO's orbital inclination. See (*10*).
18. R. C. Weast, *CRC Handbook of Chemistry and Physics* (CRC Press, Boca Raton, FL, ed. 55, 1974).
19. C. Newman, S. Lewis, P. Read, *Icarus* **174**, 135 (2005).
20. R. M. Haberle, J. R. Murphy, J. Schaeffer, *Icarus* **161**, 66 (2003).
21. J. Laskar *et al.*, *Icarus* **170**, 343 (2004).
22. R. Haberle *et al.*, *J. Geophys. Res.* **106**, 23317 (2001).

Acknowledgments: K. Herkenhoff and C. Fortezzo provided useful comments on an earlier version of the paper. Remarks by three anonymous referees were exceedingly helpful. Funding for this work was provided by the NASA MRO project. The radar and imaging data are available through NASA's Planetary Data System.

Supporting Online Material

www.sciencemag.org/cgi/content/full/science.1203091/DC1
Materials and Methods
SOM Text
Figs. S1 to S5
Tables S1 to S4
References

20 January 2011; accepted 23 March 2011
Published online 21 April 2011;
10.1126/science.1203091

Late Mousterian Persistence near the Arctic Circle

Ludovic Slimak,[1]* John Inge Svendsen,[2] Jan Mangerud,[2] Hugues Plisson,[3] Herbjørn Presthus Heggen,[2] Alexis Brugère,[4] Pavel Yurievich Pavlov[5]

Palaeolithic sites in Russian high latitudes have been considered as Upper Palaeolithic and thus representing an Arctic expansion of modern humans. Here we show that at Byzovaya, in the western foothills of the Polar Urals, the technological structure of the lithic assemblage makes it directly comparable with Mousterian Middle Palaeolithic industries that so far have been exclusively attributed to the Neandertal populations in Europe. Radiocarbon and optical-stimulated luminescence dates on bones and sand grains indicate that the site was occupied during a short period around 28,500 carbon-14 years before the present (about 31,000 to 34,000 calendar years ago), at the time when only Upper Palaeolithic cultures occupied lower latitudes of Eurasia. Byzovaya may thus represent a late northern refuge for Neandertals, about 1000 km north of earlier known Mousterian sites.

Most of the Russian Arctic was free of glacier ice throughout the past 50,000 years, including during the Last Glacial Maximum (LGM) (*1*). A varied herbivorous fauna existed in high Arctic areas that are presently wet tundra or almost barren Arctic deserts (*2*). Recent archaeological evidence demonstrates that Ice Age humans also at least temporarily lived and hunted in these northern landscapes beginning around 35,000 to 36,000 ^{14}C years before the present (yr B.P.) [≥40,000 yr B.P. in calibrated/calendar (cal) years] (*3*–*7*) (fig. S1). It has not been clear whether the early visitors were members of a fossil population [such as *Homo sapiens neanderthalensis* and affiliated groups (*8*, *9*)] or whether modern humans (*H. sapiens sapiens*) expanded northward into a previously uninhabited area.

This question is related to the Middle Palaeolithic (MP) to Upper Palaeolithic (UP) cultural transition in Eurasia. This transition, which has been considered to have taken place about 40,000 to 37,000 yr B.P. in most of Eurasia, saw the global extinction of the Neandertals and thus the end of their specific MP (Mousterian) culture. The Neandertals were replaced by modern humans, who were the bearers of all known UP cultures.

Here we describe lithic technology and age constraints from the Byzovaya site near the Polar Urals and show that humans bearing MP stone technology persisted to 32,000 to 34,000 cal yr B.P. in the Eurasian Arctic (Fig. 1). Byzovaya, which is among the northernmost known Palaeolithic sites, was previously considered to be an Early Upper Palaeolithic (EUP) site mainly on the basis of a few radiocarbon dates that suggested an age of about 27,000 ^{14}C years or younger.

The Byzovaya site (65°01′25″N, 57°25′12″E) is located on the right bank of the Pechora River, which flows northward across the lowland areas west of the Ural Mountains (Fig. 1). First described in 1965 by Guslitser *et al.* (*10*), the locality was investigated several times by Russian archaeologists (*11*); later by a Norwegian-Russian team, since 1996 (*6*, *12*); and by a French-Russian team since 2007. More than 300 stone artefacts and 4000 animal remains have been uncovered during the various excavations, which together cover an area of approximately 550 m^2.

[1]CNRS, UMR 5608, TRACES, Université de Toulouse le Mirail, Maison de la Recherche, 5 Allées Antonio Machado, 31058 Toulouse Cedex 9, France. [2]Department of Earth Science and Bjerknes Centre for Climate Research, University of Bergen, Allégaten 41, N-5007, Bergen, Norway. [3]CNRS, UMR 5199, PACEA, IPGQ, Université Bordeaux 1, Bâtiment B18, Avenue des Facultés, 33405 Talence Cedex, France. [4]CNRS, USR 3225 and UMR 7041, ArScAn, "Archéologies Environnementales," Maison de l'Archéologie et de l'Ethnologie René Ginouvès, CC023, 21, Allée de l'Université, 92023 Nanterre Cedex, France. [5]Department of Archaeology, Institute of Language, Literature and History, Komi Science Centre, Russian Academy of Sciences, Kommunisticheskaya Street 26, 167000 Syktyvkar, Komi, Russia.

*To whom correspondence should be addressed. E-mail: slimak@univ-tlse2.fr

www.sciencemag.org/cgi/content/full/science.1203091/DC1

Supporting Online Material for

Massive CO_2 Ice Deposits Sequestered in the South Polar Layered Deposits of Mars

Roger J. Phillips,* Brian J. Davis, Kenneth L. Tanaka, Shane Byrne, Michael T. Mellon, Nathaniel E. Putzig, Robert M. Haberle, Melinda A. Kahre, Bruce A. Campbell, Lynn M. Carter, Isaac B. Smith, John W. Holt, Suzanne E. Smrekar, Daniel C. Nunes, Jeffrey J. Plaut, Anthony F. Egan, Timothy N. Titus, Roberto Seu

*To whom correspondence should be addressed. E-mail: roger@boulder.swri.edu

Published 21 April 2011 on *Science* Express
DOI: 10.1126/science.1203091

This PDF file includes:

Materials and Methods
SOM Text
Figs. S1 to S5
Tables S1 to S4
References

Supporting Online Material for

Massive CO_2 Ice Deposits Sequestered in the South Polar Layered Deposits of Mars

Roger Phillips,[1*] Brian J. Davis,[2,3] Kenneth L. Tanaka,[4] Shane Byrne,[5] Michael T. Mellon,[6] Nathaniel E. Putzig[2], Robert M. Haberle,[7] Melinda A. Kahre,[8] Bruce A. Campbell,[9] Lynn M. Carter,[10] Isaac B. Smith,[11] John W. Holt,[11] Suzanne E. Smrekar,[12] Daniel C. Nunes,[12] Jeffrey J. Plaut,[12] Anthony F. Egan,[13] Timothy N Titus,[4] Roberto Seu[14]

[1]Planetary Science Directorate, Southwest Research Institute, Boulder, CO 80302, USA and Department of Earth and Planetary Sciences, Washington University, St. Louis, MO 63130 USA. [2]Department of Space Studies, Southwest Research Institute, Boulder, CO 80302, USA. [3]Now at Department of Geophysics, Colorado School of Mines, Golden, CO, 80401, USA. [4]Astrogeology Science Center, U.S. Geological Survey, Flagstaff, AZ 86001, USA. [5]Lunar and Planetary Laboratory, University of Arizona, Tucson, AZ 85721, USA. [6]Laboratory for Atmospheric and Space Physics, University of Colorado, Boulder, CO 80303, USA. [7]Space Science and Astrobiology Division, NASA Ames Research Center, Moffett Field, CA 94035, USA. [8]Bay Area Environmental Research Institute / NASA Ames Research Center, Moffett Field, CA 94035, USA. [9]Center for Earth and Planetary Studies, Smithsonian Institution, Washington, DC 20013, USA. [10]Science and Exploration Directorate, NASA Goddard Space Flight Center, Greenbelt, MD 20771, USA. [11]Institute for Geophysics, Jackson School of Geosciences, University of Texas, Austin, TX 78758, USA. [12]Jet Propulsion Laboratory, California Institute of Technology, Pasadena, CA 91109, USA. [13]Department of Space Operations, Southwest Research Institute, Boulder, CO 80302, USA. [14]Sapienza University of Rome, Department of Information Engineering, Electronics and Telecommunications, 18-00184, Rome, Italy

*To whom correspondence should be addressed. E-mail: roger@boulder.swri.edu

This PDF file includes:

SOM Methods and Supporting Text
SOM References
Figs. S1 to S5
Tables S1 to S4

Methods and Supporting Text

1. SHARAD Data Selection for Permittivity Analyses of the RFZ_3 Volume

For the Martian south polar layered deposits (SPLD), we examined Shallow Radar (SHARAD) data from 129 orbits in a seismic data analysis package (furnished by SeisWare Inc.). Reflection-free zones (RFZ) were mapped in 118 of these orbits (Fig. S1, Table S1). Processed radar signals are displayed as radargrams, which are two-dimensional power images in time delay vs. spacecraft orbit position. RFZ_3 deposits are seen in 79 SHARAD radargrams and have locales poleward of ~85°S over an area spanning ~120° of longitude (~235°–355°E) in the SPLD. However, a radargram is only suitable for estimating real permittivity, ε', (Fig. S2) if the RFZ_3 basal boundary, LB_3, is bright, continuous, and topographically varied. Furthermore, within the organized sequence of layered radar reflectors (ORR) beneath the RFZ_3, there must be at least one well-resolved reflection (the test reflector). The topographic variability of the RFZ_3 base ensures that a deeper reflector is distorted when converting from time to depth if an incorrect permittivity is assumed for RFZ_3. Accounting for these requirements, 41 of the 79 orbits were suitable for analysis (see Table S2). For different strategies (see below), orbit-specific ε' estimates were used to obtain mean values of real permittivity for the entire RFZ_3 deposit. From this, specific mean values of ε' for RFZ_3 were used in time-to-depth conversions of that zone, while other volumes were assigned a permittivity of water ice.

2. Time-to-Depth Conversions

For each radargram used in the analysis, the delay times to five horizons (Fig. S2) were mapped using the SeisWare software package. From top to bottom, these are: (*i*) the exposed surface, (*ii*) the top of the thin layer that typically bisects RFZ_3 (bisecting layer, BL), (*iii*) the bottom of the BL, (*iv*) the RFZ_3 basal reflector (LB_3), and (*v*) the deeper test reflector used for the permittivity estimates. The thickness of each layer defined by any two successive horizons was then calculated by converting the time-delays to depths on a frame-by-frame basis using $\Delta d_{ij} = C_0 \Delta t_{ij} / 2\sqrt{\varepsilon_{ij}}$, where C_0 is the speed of light in free space, Δt_{ij} is the incremental time delay, ε_{ij} is the real permittivity, and Δd_{ij} is the thickness of the layer between horizons j and j+1 in the ith radar frame. The division by 2 accounts for the two-way travel time of the radar signal. A "frame" can be considered to be a single trace of power vs. time; the amalgamated set of frames along the orbital ground track make up the radargram. By bookkeeping horizons independently, we were able to assign different permittivities to the specific intervals between any two horizons. We used two different though related methods to analyze the dielectric properties of the RFZ_3 material and determine a likely permittivity value: a correlation method and a regression method.

3. Estimating ε': Correlation Method

Because subsurface reflectors detected by SHARAD are typically smooth at the scales of the radar's wavelengths, it is impractical to use refractive-index information captured in the Doppler frequency spectrum (*S1*) to estimate subsurface velocity, hence real permittivity. However, a method was developed to estimate the permittivity of RFZ_3 by taking advantage of layer geometry. The radar stratigraphy is an organized sequence of layered radar reflectors (ORR) overlain by a several-hundred-meter thick region of unorganized, weak radar reflectors (WRR), which in turn are overlain by RFZ_3. ORR is very likely the lateral extension of the layered depositional unit that is well exposed in the Promethei Lingula area on the perimeter of the SPLD and that is inferred by outcrop correlations to extend under the entire SPLD (*S2*). The layering is clearly apparent in SHARAD radar data in the Promethei Lingula region (*S3, S4*) and can be traced in SHARAD radargrams from Promethei Lingula to beneath RFZ_3 (*S5*). The likely geological progression in the RFZ_3 region was: (*i*) deposition of ORR, (*ii*) deposition of WRR, (*iii*) erosion of WRR, and (*iv*) deposition of RFZ_3 onto the eroded surface of WRR. We do not expect any correlation between the shapes of the ORR reflectors in the older depositional sequence and the shape of the younger erosional surface, LB_3, at the base of RFZ_3 (Fig. S2). Fortuitous correlations will result, however, from an incorrect assignment of the RFZ_3 permittivity. For example, in radargrams where time delay has been converted to depth by assuming a permittivity (i.e., wave speed) of water ice, there is a significant anticorrelation between LB_3 and the ORR sequence of layers (Fig. 2A, main text). If within just the RFZ_3 volume we systemically lower ε' from its water-ice value of 3.15, the negative correlation coefficient between LB_3 and the test reflector (typically the uppermost reflector in the ORR sequence) increases, passes through zero, and then becomes positive (Fig. 2C, main text).

The correlative relationship between LB_3 (red line, Fig. S2) and the underlying test reflector (orange line, Fig. S2) was determined by extracting the relevant information from the SeisWare environment and calculating in MATLAB the correlation coefficient, *r*, between the two data sets where they coincided in lateral position. In the nominal procedure of converting time to depth, all volumes except RFZ_3 had $\varepsilon' = 3.15$ (water ice). Varying the real permittivity of RFZ_3 affected the shape of both the basal and test reflectors, and we varied this quantity systematically (Figs. 2B, 2C, main text) until *r* was found to be zero to at least two decimal places for each of the 41 orbital observations. That is, we sought the value of permittivity that maximally decorrelated the test reflector and LB_3. Note that this procedure yields the effective mean value of the RFZ_3 ε' along a given orbit observation sequence across RFZ_3. This is also the vertically-averaged value of ε' in the sense that for a given thickness, the same radar time delay in RFZ_3 will result from both the mean value and the real vertical profile of permittivity.

We applied the correlation technique two different ways: (*i*) by assuming that the chosen permittivity applied to the entire RFZ_3 volume, and (*ii*) by assuming that the thin bisecting layer represents a depositional episode of water ice and has a permittivity of 3.15, with the rest of the volume used for ε' estimation. These two methods yield mean permittivity estimates of 2.1 ± 0.2 and 2.0 ± 0.2, respectively (see Table S2). An outlier of RFZ_3 (Fig. S2, highest exposure of RFZ_3) may unduly influence the correlation coefficient calculation; excluding these data raised the permittivity estimates to 2.2 ± 0.2 in both cases.

4. Estimating ε': Regression Method

Our experience with radar reflectors in the Martian polar deposits is that they are reasonably smooth at the scale of tens of kilometers unless disrupted by significant short-wavelength erosional processes. The radar layering in the Promethei Lingula region, the conjectured extension of our ORR sequence, is sub-horizontal and only occasionally exhibits gently dipping angular unconformities (*S3, S4*). An alternative scheme for estimating the RFZ_3 mean value of ε' was therefore based on finding the permittivity value for each radargram that with a linear least-squares fit minimized the standard deviation of topographic undulations on the test reflector in the ORR (Figs. 2D, 2E, main text). This approach yields a value of 2.2 ± 0.1 (both with and without the BL; see Table S2), similar to the correlation results. The regression was sensitive to two aspects of the test-reflector shape that result from an incorrect choice of ε' in RFZ_3: (*i*) apparent undulations within the test reflector and (*ii*) an apparent offset in the test reflector associated with the outlier mentioned above (Fig S2). The best fitting solutions tended to minimize both the offset and the undulations (Fig. 2E, main text). In actuality, the apparently offset test reflector is continuous, but portions of this connection could not be reliably mapped for analysis purposes (Fig. S2).

5. Thickness and Interpolated Volume Estimates

Having estimated mean permittivities for RFZ_3, we converted time delays to thicknesses using ε' = 2.0, 2.1, and 2.2. Fig. S3 shows RFZ_3 thickness variations along individual orbital tracks for ε' = 2.1, where the BL has been included in the calculation. Volume estimates were achieved by interpolating between orbital track data. We interpolated within closed areas, and avoided natural breaks in the data, such as across troughs. Table S3 gives the interpolated area of RFZ_3, and for each of the three permittivities, the average thickness and volume with and without the BL included.

6. Extrapolated Volume and Mass of RFZ_3

We used the AA_3 areal distribution to extrapolate the RFZ_3 volume, including that within the region poleward of ~87°S where SHARAD data are unavailable. We multiplied the estimated RFZ_3 volumes (with and without the BL) by the ratio of the AA_3 area to the RFZ_3 area, resulting in a volume of ~12,500 km^3 with the BL included (Table S4). To achieve a more conservative value, we extrapolated the RFZ_3 thicknesses by a minimum curvature method constrained by the AA_3 boundaries (Fig. S4), and we note that excluding the north-trending AA_3 lobes where RFZ_3 was not mapped decreased the answer by less than 3%. With this approach, we estimate a volume of 9,500 km^3 with the BL excluded, approximately twice the directly mapped RFZ_3 volume.

A conversion of volume to mass is necessary to compare the RFZ_3 CO_2 reservoir to the present atmospheric mass. Annual CO_2 deposits on Mars have been observed to metamorphose to slab CO_2 ice over the course of a winter (*S6, S7*), indicating that perennial CO_2 deposits should be very dense with little porosity. The lack of a positive trend of ε' values with thickness (see below), as well as the permittivity estimates themselves, support this view. Thus we adopt a density range close to solid dry ice, 1500-1600 kg m^{-3} (*S8*), yielding an atmospheric-equivalent pressure of 4-5 mbar over the volume range 9,500-12,500 km^3.

7. Porous Water-Ice Hypothesis

Porous water ice is an alternative hypothesis to our CO_2 interpretation of the low ε' values. A mixture of solid water ice (ε' = 3.15) and void space (ε' = 1.0) would match our permittivity estimates with the proper choice of porosity (~40%). We tested this hypothesis by examining how the permittivity results behave as a function of thickness, which is just integrated depth. The porous water-ice hypothesis would predict a positive slope in a plot of ε' versus thickness. Figure S5 shows the ε' values estimated by the correlation coefficient method plotted as a function of thickness. The results are somewhat scattered, and a straight-line fit to the data yields essentially a zero slope and an insignificant correlation coefficient of +0.03. Applying the same test to the regression-derived values yields similar results.

We examined models of ice densification with depth and converted them to permittivity versus thickness for comparison with SHARAD results. Antarctica can be used as an analog for Mars, as ice densification is largely a dry-based process in both locales, with melting and refreezing unimportant. While temperatures are lower in the SPLD than Antarctica, RFZ_3 has very likely been in place longer than the near subsurface ice of Antarctica, and time can be traded off with temperature in sintering processes that densify water ice. It is estimated that the oldest firn air (at pore close-off depth) on the Antarctic continent is 156 ± 22 years (*S9*). We contend that RFZ_3 is older (stratigraphically lower) than the water-ice layer that makes up the lower unit of the south pole residual cap (SPRC) and is estimated to have been deposited ~20,000 years ago, when Mars perihelion coincided with summer in the northern hemisphere (*S10*). We adopted the model of Salamatin and Lipenkov (*S11*), which provides a very good fit to density vs. depth data in ice cores from Antarctica, and we scaled the depth dependence by the ratio of Mars to Earth gravity (*S12*). The resulting density profile was used to construct a model of real permittivity vs. depth using the Tinga-Voss-Blossey dielectric mixing formula (spherical inclusions) (*S13*). Fig. S5 shows the model prediction using parameters determined from ice core data taken at east Dronning Maud Land, Antarctica (*S11*). Note that we converted the depth results to average ε'

values vs. thickness by calculating the mean ε' value above any given depth. The porous water-ice model not only has ε' values significantly higher than our RFZ_3 estimates, but also has a strong positive trend that is not observed in the RFZ_3 results. A theoretical densification model applied specifically to the north polar cap of Mars (*S14*) was also used to generate permittivity-thickness relationships. This model generates curves with a slightly stronger positive trend and lower values of permittivity than the gravity-scaled Antarctic model, but the solutions are well outside the 95% confidence limits of the data fits (Fig. S5). Thus both the data themselves and the models strongly suggest that porous water ice is an untenable hypothesis for explaining the low ε' values estimated from SHARAD.

Supporting Online Material References

S1. F. Heliere, C.-C. Lin, H. Corr, D. Vaughan, Radio echo sounding of Pine Island Glacier, West Antarctica: Aperture synthesis processing and analysis of feasibility from space. *IEEE Transactions on Geoscience and Remote Sensing* **45**, 2573 (2007).

S2. S. M. Milkovich, J. J. Plaut, Martian South Polar Layered Deposit stratigraphy and implications for accumulation history. *J. Geophys. Res.* **113**, E06007 (2008).

S3. R. Seu *et al.*, Accumulation and erosion of Mars' South Polar Layered Deposits. *Science* **317**, 1715 (2007).

S4. S. M. Milkovich *et al.*, Stratigraphy of Promethei Lingula, south polar layered deposits, Mars, in radar and imaging data sets. *J. Geophys. Res.* **114**, E03002 (2009).

S5. R. J. Phillips *et al.*, Subsurface structure of the South Polar Layered Deposits, Mars. *LPSC XL*, 2007.pdf (2009).

S6. T. N. Titus, H. H. Kieffer, K. F. Mullins, P. R. Christensen, TES premapping data: Slab ice and snow flurries in the Martian north polar night. *J. Geophys. Res.* **106**, 23,181 (2001).

S7. S. Cull *et al.*, Seasonal H_2O and CO_2 ice cycles at the Mars Phoenix landing site: 1. Prelanding CRISM and HiRISE observations. *J. Geophys. Res.* **115**, E00D16 (2010).

S8. R. C. Weast, *CRC handbook of Chemistry and Physics*. (CRC Press, Inc, Boca Raton, FL, ed. 55, 1974).

S9. K. Kaspers *et al.*, Model calculations of the age of firn air across the Antarctic continent. *Atmospheric Chemistry and Physics* **4**, 1365 (2004).

S10. F. Montmessin *et al.*, On the origin of perennial water ice at the south pole of Mars: A precession-controlled mechanism? *J. Geophys. Res.* **112**, E08S17 (2007).

S11. A. Salamatin, V. Lipenkov, Simple relations for the close-off depth and age in dry-snow densification. *Annals of Glaciology* **49**, 71 (2008).

S12. M. Carr, J. Head III, Basal melting of snow on early Mars: A possible origin of some valley networks. *Geophys. Res. Lett.* **30**, 2245 (2003).

S13. F. T. Ulaby, R. K. Moore, A. K. Fung, *Microwave Remote Sensing, Active and Passive, Vol. III*. (Artech House, Norwood, MA, 1986), pp. 2162.

S14. R. J. Arthern, D. P. Winebrenner, E. D. Waddington, Densification of water ice deposits on the residual north polar cap of Mars. *Icarus* **144**, 367 (2000).

S15. E. J. Kolb, K. L. Tanaka, R. Greeley, G. Neukum, the HRSC Co-Investigator Team, The residual ice cap of Planum Australe, Mars: New insights from the HRSC experiment. *LPSC XXXVII*, 2408.pdf (2006).

S16. K. L. Tanaka, E. Kolb, C. Fortezzo, Recent advances in the stratigraphy of the polar regions of Mars. *Seventh International Conference on Mars*, 3276.pdf (2007).

Supporting Online Material Figures

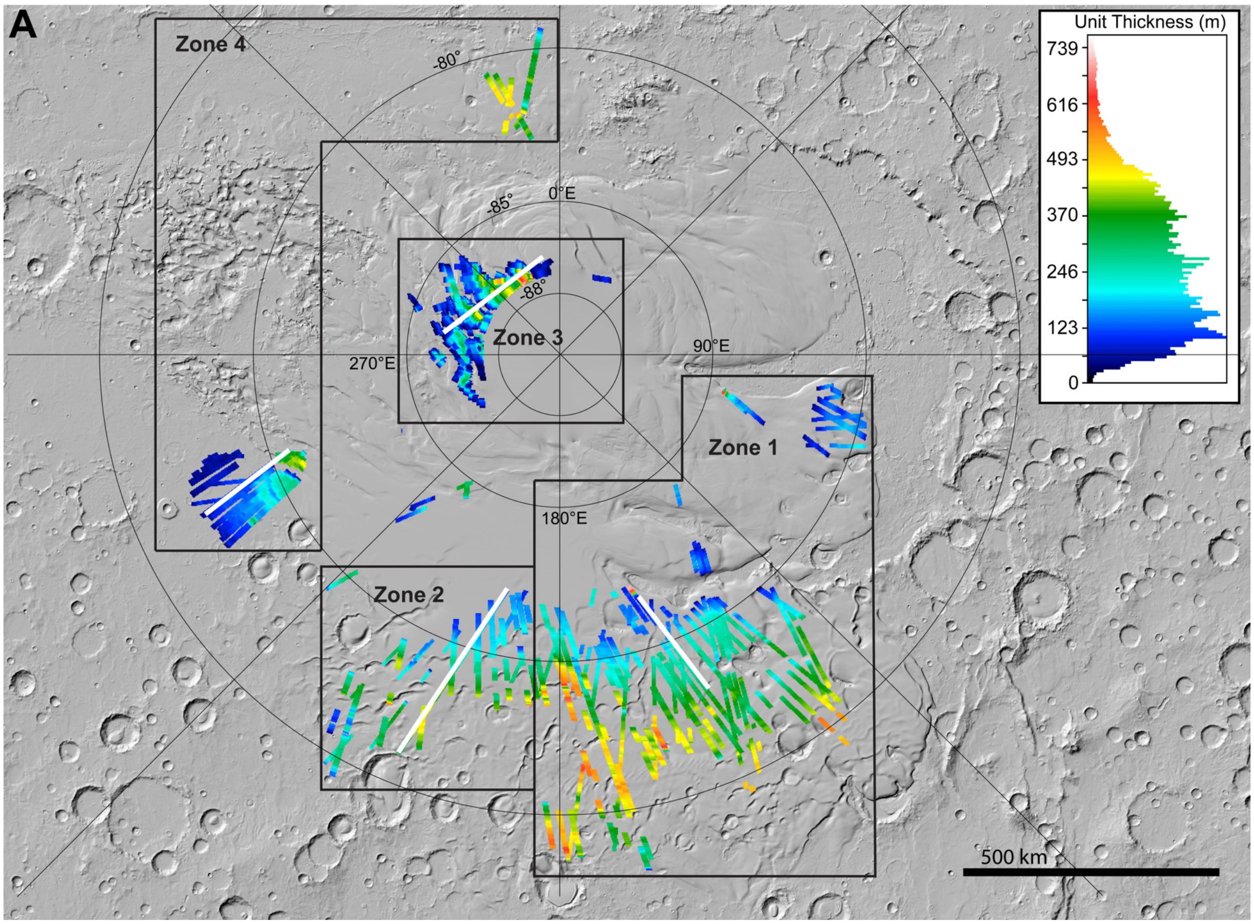

Figure S1. (**A**) Polar stereographic map of the south polar region of Mars, showing where reflection-free zones (RFZ) were mapped on 118 SHARAD ground tracks, overlain on a Mars Orbiter Laser Altimeter (MOLA) shaded relief map. These RFZs were subdivided into four regions based on qualitative differences in their radar characteristics (Table S1). We searched the entire SPLD for RFZs, so the four groups represent the sum total for the SPLD. The unclassified data poleward of Zone 2 are ambiguous but most closely resemble radargrams in RFZ_2. Except for RFZ_3, we did not process all orbits within each RFZ, and this is reflected in gaps between mapping strips. The ribbon color along orbital tracks indicates radar unit thickness (see histogram) calculated using an assumed real permittivity, ε', of 3.15 (water ice), as we do not know the composition of zones 1, 2 and 4. Because we conclude that zone 3 has a permittivity of ~2.1 (interpreted as CO_2 ice), the thicknesses there in actuality should be scaled by $\sim\sqrt{3.15/2.1}$. The histogram shows relative occurrence of thicknesses. (**B**) A typical radargram is shown for each region, and a white line on the map (A) marks each location.

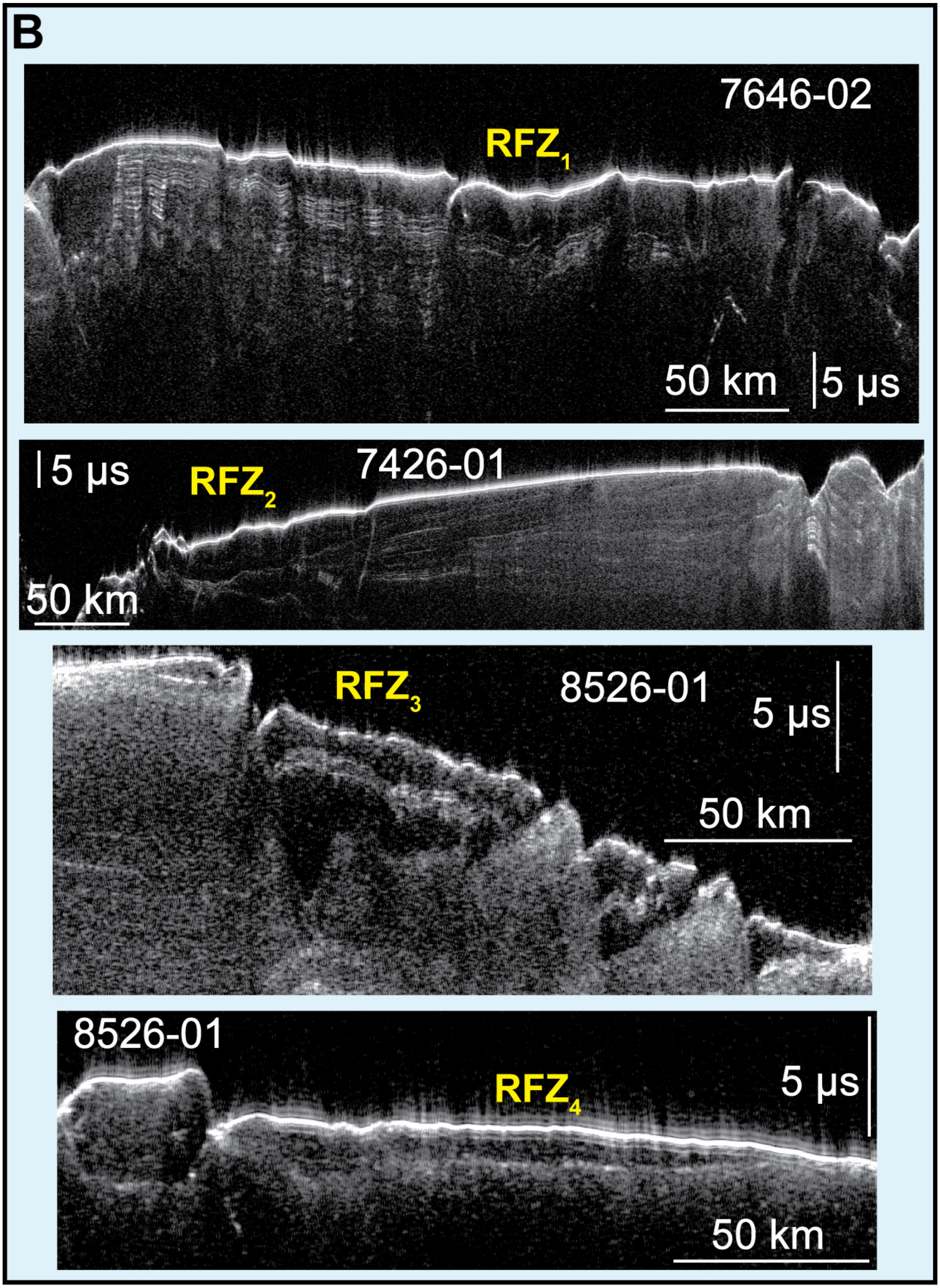
B
7646-02
RFZ1
50 km
5 μs
5 μs
RFZ2
7426-01
50 km
RFZ3
8526-01
5 μs
50 km
8526-01
RFZ4
5 μs
50 km

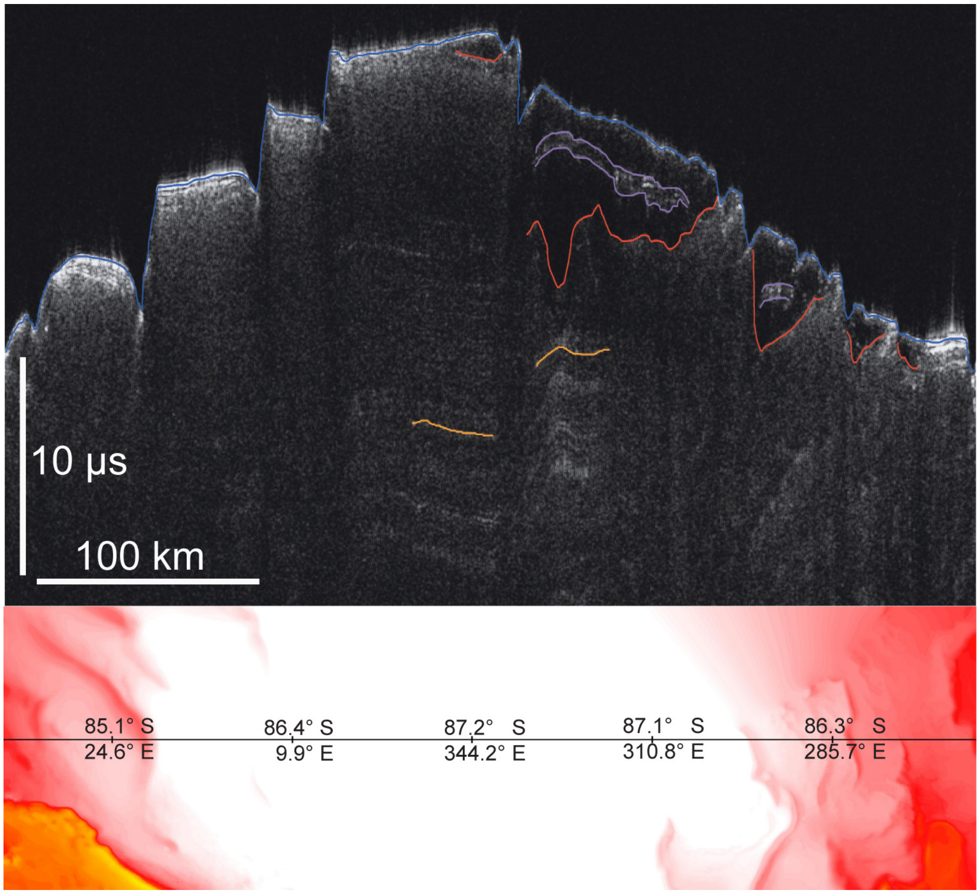

Figure S2. SHARAD radargram for orbit 8104-01 over the RFZ_3 unit. In each of the 41 radargrams used for permittivity analysis, the time-delays to five reflectors were measured: (*i*) the surface of the SPLD (blue trace); (*ii* and *iii*) the top and bottom of the bisecting layer (BL, purple traces); (*iv*) the basal interface, LB_3, between RFZ_3 and the underlying SPLD material (red trace); and (*v*) the "test" reflector from the underlying ORR layer sequence (orange trace). These time-delays were converted to depths, varying the permittivity of the RFZ_3 sequence systematically to find both the value that resulted in a zero linear correlation coefficient between the orange and red traces and the value that minimized the standard deviation of the residuals of a straight line fit to the orange trace. In an alternative procedure, the bisecting layer was assigned $\varepsilon' = 3.15$ (water ice), and the inversions were carried out on the remainder of RFZ_3.

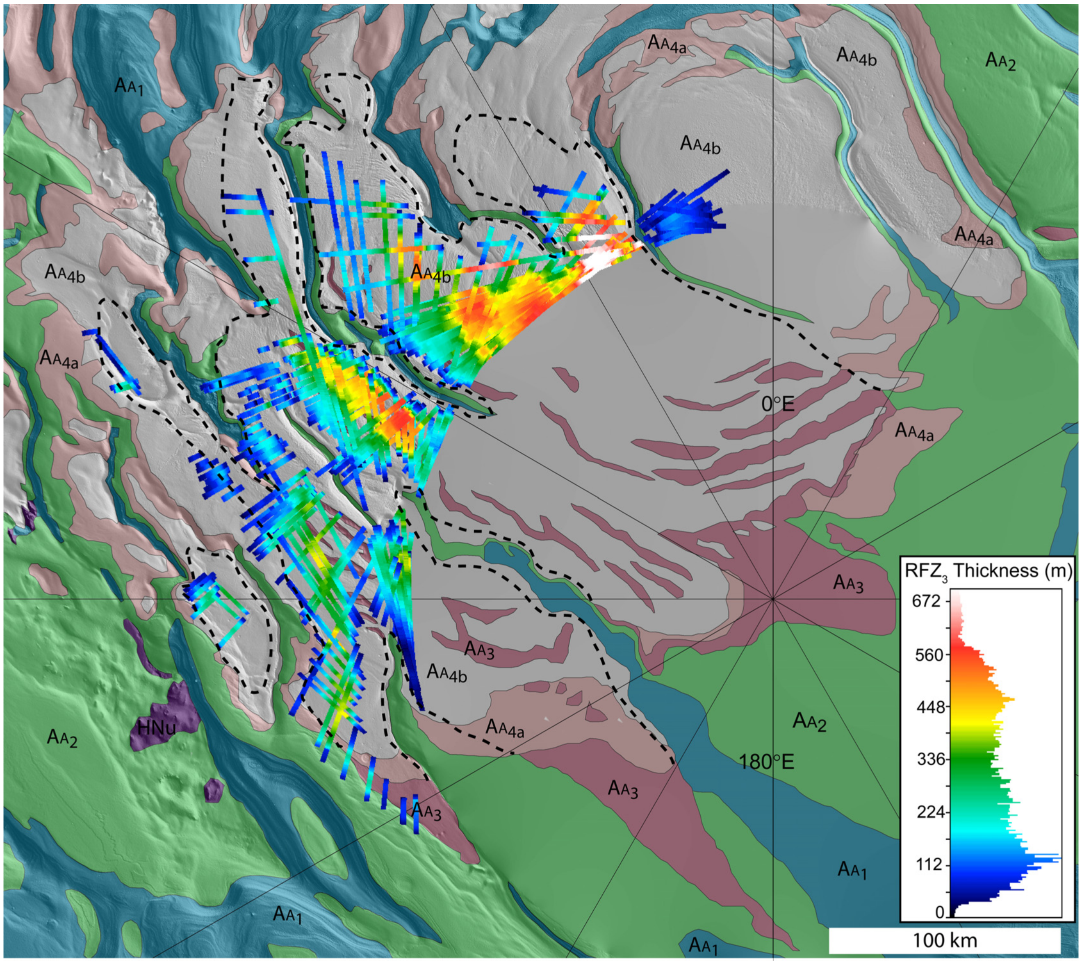

Figure S3. Polar stereographic map of Mars's south polar region, showing where RFZ$_3$ deposits were mapped along 79 SHARAD ground tracks. The ribbon colors indicate RFZ$_3$ unit thicknesses calculated using 2.1 for the real permittivity. See histogram, which shows relative occurrence of thicknesses. SHARAD results are overlain on a map showing SPLD stratigraphy (S*15,* S*16*). Geologic units are: AA$_1$ (evenly bedded layers, making up most of the SPLD deposits and reaching a maximum thickness of >3.5 km); AA$_2$ (consists of evenly bedded layers and is <300 m thick); AA$_3$ (occurs only in the summit area of the SPLD, is ~300 m thick, lies unconformably over units AA$_1$ and AA$_2$, consists of 6-7 conformable layers, and has a low-to-intermediate albedo); and AA$_{4a}$ and AA$_{4b}$ [water-ice and CO_2-ice members, respectively, of the south pole residual cap (SPRC)]. HNu is stratigraphically undivided material lying beneath the SPLD. The areas enclosed by the dashed lines indicate the continuation of the AA$_3$ unit where it is mostly buried by the SPRC, and the locations are well constrained by AA$_3$ exposures in troughs and elsewhere.

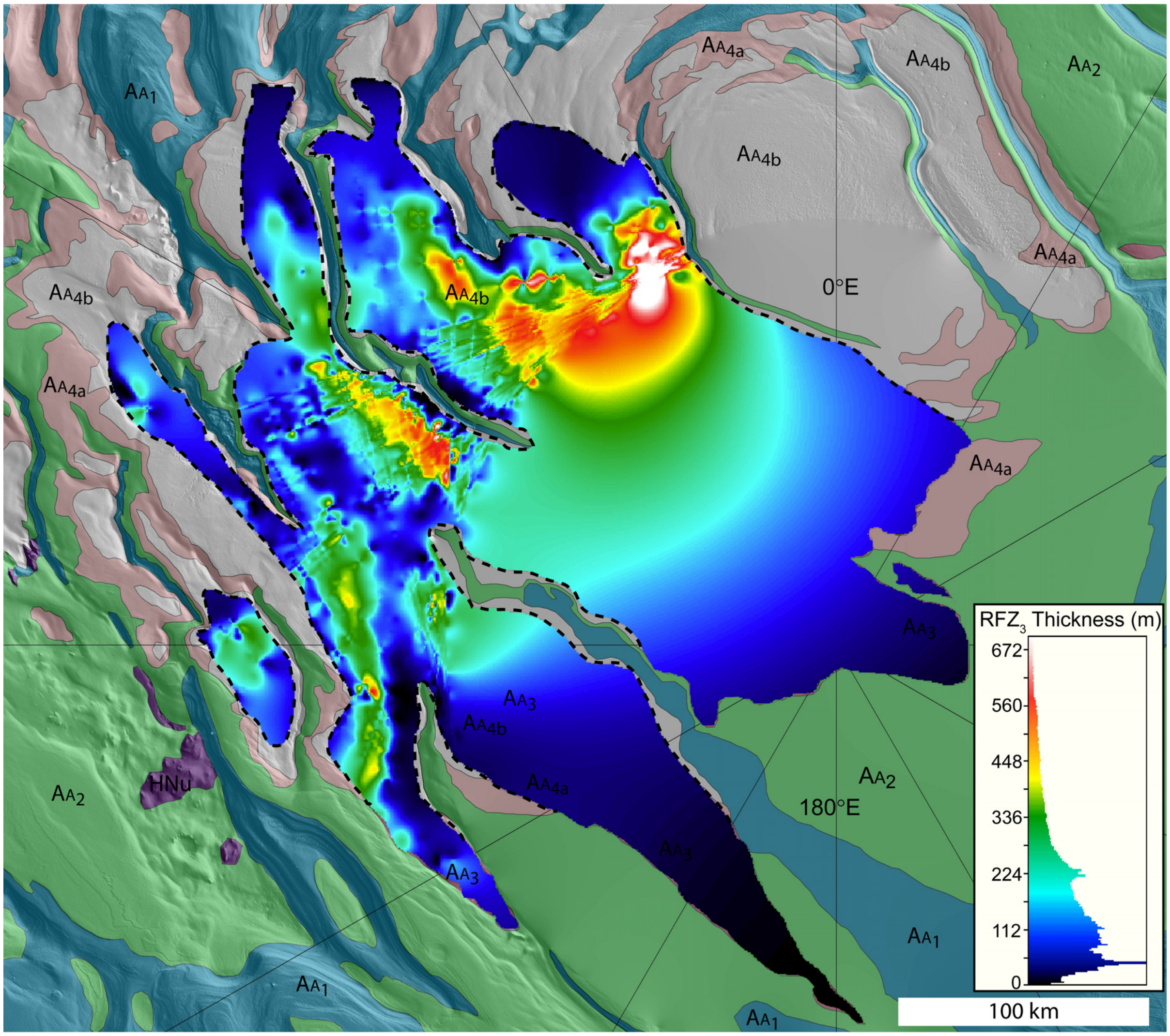

Figure S4. Thickness data from the SHARAD-mapped RFZ_3 unit (calculated using $\varepsilon' = 2.1$) extrapolated over and constrained by the areal extent of the AA_3 unit. The extrapolation was computed in SeisWare using a minimum-curvature interpolation function. The histogram shows relative occurrence of thicknesses.

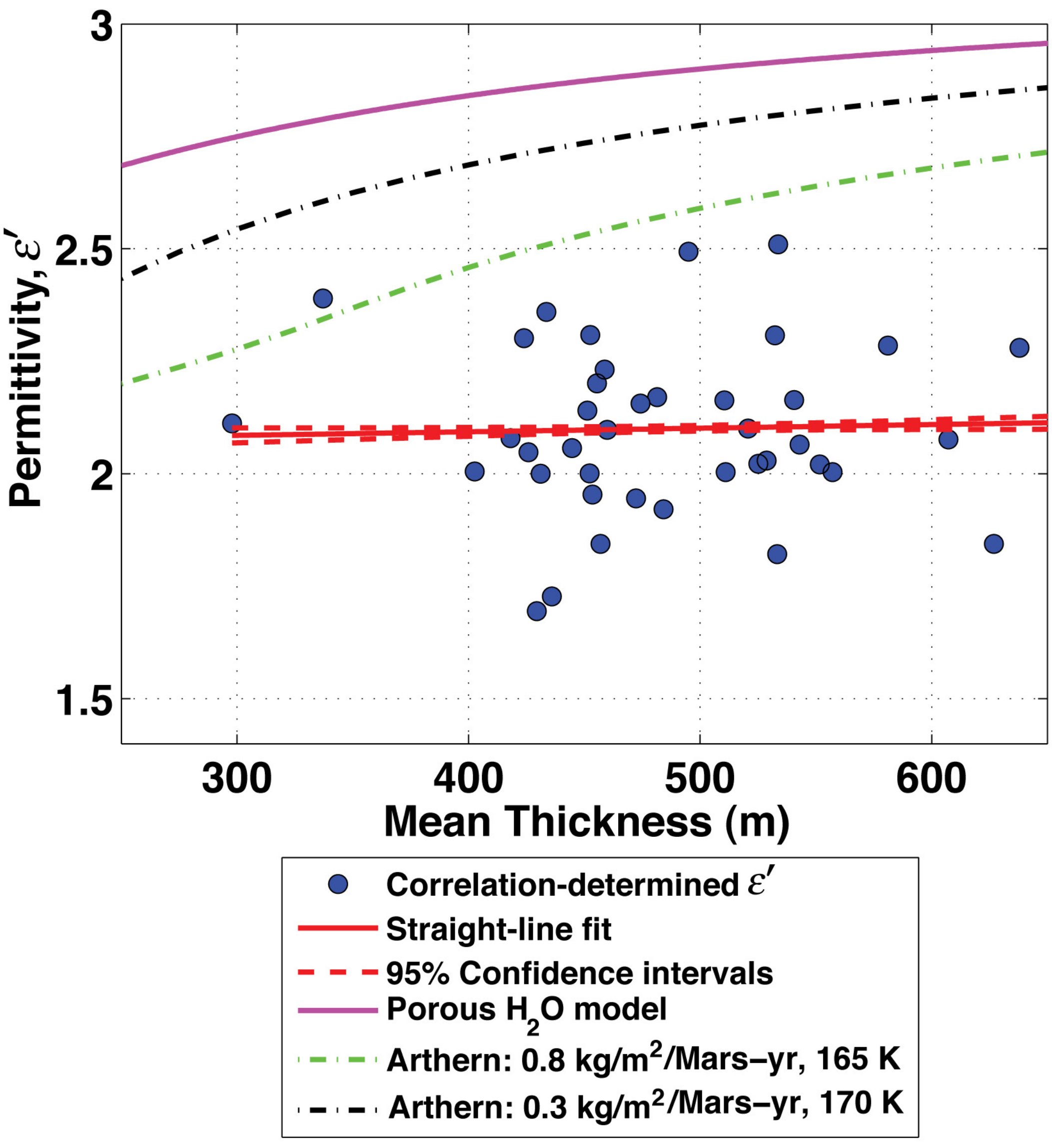

Figure S5. Diagram of permittivity, ε', versus mean thickness. Scatter points represent values determined from the correlation method along each of the 41 orbital tracks, with the bisecting layer included in the estimation. A straight-line fit to the data is shown along with the 95% confidence limits. The permittivity based on the gravity-scaled densification model of Salamatin and Lipenkov (S*11*) is plotted against thickness ("Porous H_2O model"). Also shown are permittivity-thickness relationships derived from a Mars-specific densification model (S*14*) for two combinations of mass accumulation rate and mean annual surface temperature.

Supporting Online Material Tables

	RFZ characteristics	Underlying material characteristics	Location
RFZ_1	Very few internal reflections	A series of bright, finely-spaced reflectors known as the Promethei Lingula layer sequence (S*2,* S*3,* S*4*).	~90°E–180°E
RFZ_2	Scattered, low-power hints of layering near the RFZ base.	Radar layering is poorly resolved and weaker than that beneath RFZ_1. In some cases, primarily the northern edge of the zone, there are no underlying reflections at all.	180°E–225°E
RFZ_3	Other than a thin layer that typically bisects the RFZ, almost completely devoid of reflectors.	A very poorly resolved, faint stack of reflectors, in turn overlying a bright packet of reflectors.	~235°E–355°E; south of ~85°S
RFZ_4	Some faint layering.	No sign of layering but evidence of volume or interior surface scattering. May be Noachian/Hesperian basement beneath the SPLD.	Outliers near ~270°E–0°E and ~240°E–250°E

Table S1. Radar characteristics of reflection free zones (RFZ) and material beneath.

	BL considered part of RFZ_3		BL has ε' = 3.15	
Observation	ε' from correlation	ε' from regression	ε' from correlation	ε' from regression
4517-01	2.494	2.298	2.501	2.242
4728-01	2.185	2.259	2.215	2.233
5216-01	1.695	2.108	1.540	2.083
5572-01	1.727	2.046	1.572	2.015
5783-01	2.001	2.136	1.848	2.083
5968-01	2.36	2.154	2.271	2.131
5994-01	2.022	2.311	1.911	2.275
6139-01	2.510	2.300	2.496	2.265
6561-01	1.946	2.279	1.862	2.279
6772-01	1.844	2.021	1.702	2.012
6838-01	2.021	2.099	1.911	2.049
6983-01	1.844	2.110	1.723	2.032
7049-01	2.170	2.241	2.032	2.212
7194-01	2.057	2.280	1.934	2.261
7260-01	2.308	2.413	2.195	2.374
7471-01	2.097	2.118	1.949	2.066
7484-01	2.004	2.193	1.902	2.197
7616-01	1.921	2.062	1.751	1.995
7682-01	2.156	2.312	2.060	2.311
7827-01	2.232	2.259	2.126	2.24
7893-01	2.000	2.164	1.872	2.156
7905-01	2.112	2.652	1.994	2.642
8038-01	2.302	2.272	2.197	2.271
8104-01	2.048	2.114	1.909	2.08
8526-01	2.140	2.135	1.991	2.079
8671-01	2.390	2.319	2.301	2.292
8737-01	1.954	2.006	1.810	1.945
8948-01	2.309	2.301	2.191	2.283
9093-01	2.076	1.965	2.054	1.898
9211-01	2.100	2.260	2.026	2.236
9304-01	2.285	2.234	2.331	2.228
9370-01	1.821	2.204	1.764	2.206
9382-01	2.004	2.354	2.000	2.309
9515-01	2.079	2.302	1.955	2.339
9937-01	2.164	2.074	2.165	2.009
10068-01	2.005	2.22	1.889	2.204
12416-01	2.280	2.421	2.297	2.371
14024-01	2.029	2.070	1.883	2.058
14130-01	2.201	2.172	2.081	2.138
16121-01	2.065	2.038	1.951	2.026
16253-01	2.163	2.275	2.029	2.228
Means	**2.1 ± 0.2**	**2.2 ± 0.1**	**2.0 ± 0.2**	**2.2 ± 0.1**

Table S2. Estimates of real permittivity, ε', of RFZ_3 for 41 usable orbits as determined from correlation and regression methods. In the first two estimate columns, the bisecting layer (BL) is considered to be part of RFZ_3 in terms of permittivity. In the last two columns, the bisecting layer is assumed to represent a depositional episode of water ice with ε' = 3.15, and the permittivity is estimated for the remainder of the RFZ_3 volume. The first column is the SHARAD observation number. The means are given with their 1-σ values.

		With Bisecting Layer		Without Bisecting Layer	
RFZ_3	Area (km^2)	Avg. thickness (m)	Volume (km^3)	Avg. thickness (m)	Volume (km^3)
$\varepsilon' = 2.0$	19,976	227.3	4,541	208.8	4,170
$\varepsilon' = 2.1$	19,976	222.0	4,435	203.5	4,065
$\varepsilon' = 2.2$	19,976	216.7	4,329	198.2	3,958

Table S3. Conversion of time delays in RFZ_3 to thicknesses and volumes for three different permittivities. "With Bisecting Layer" means that the thickness and volume of the BL has *not* been subtracted from the thickness and volume of RFZ_3, and "Without Bisecting Layer" means that it has.

	With Bisecting Layer		Without Bisecting layer	
	V_{RFZ_3} (km^3)	$V_{extrapolate}$ (km^3)	V_{RFZ_3} (km^3)	$V_{extrapolate}$ (km^3)
$\varepsilon' = 2.0$	4,541	12,958	4170	11901
$\varepsilon' = 2.1$	4,435	12,656	4065	11600
$\varepsilon' = 2.2$	4,329	12,353	3958	11297

Table S4. Extrapolated RFZ_3 volume estimates are $V_{extrapolate} = (A_{AA_3}/A_{RFZ_3})\times V_{RFZ_3}$, where A_{AA_3}= 57,009 km^2 (the area of AA_3), A_{RFZ_3} = 19,976 km^2 (the area of RFZ_3), and V_{RFZ_3} is the volume estimate of RFZ_3.